Transition metal incorporation into mackinawite (tetragonal FeS)

Kideok D. Kwon[1*], Keith Refson[2,3], and Garrison Sposito[4]

[1]Department of Geology, Kangwon National University, Chuncheon 200-701, Korea

[2]STFC Rutherford Appleton Laboratory, Didcot, Oxfordshire OX11 0QX, UK

[3]Department of Physics, Royal Holloway University of London, Egham TW20 0EX, UK

[4]Geochemistry Department, Earth Sciences Division, Lawrence Berkeley National Laboratory, Berkeley, CA 94720, USA

*Email: kkwon@kangwon.ac.kr

Revision 1 for submittal to *American Mineralogist*

ABSTRACT

Naturally-occurring mackinawite (tetragonal FeS) with incorporated transition metals is an important precursor to the formation of metal sulfides in ore deposits, but experimental results have not been sufficient to establish clear trends in the structure and stability of the transition-metal-enriched mineral. Using density functional theory with dispersion corrections, we report the first systematic examination of the relationship between composition and structure for FeS incorporating bivalent transition metals. Our method was validated by successful calculations of the structures of FeS, FeSe, $FeSe_{1-x}S_x$, $Fe_{1-x}Me_xSe$ (Me = Co, Ni, Cu), and $FeNi_xTe$. Two classes of transition-metal-incorporated FeS structures then were investigated: $Fe_{1-x}Me_xS$ (metal-substituted FeS) and $FeMe_xS$ (FeS intercalated by a metal at either a tetrahedral or square-pyramidal interstitial site), where Me = Co, Ni, Cu and $x \leq 0.25$. We find that incorporated transition metals can both increase and decrease lattice parameters, depending on the metal and how it is incorporated into the FeS structure. As the mole fraction of substituting metal increases, the FeS unit cell volume decreases for Co, is nearly constant for Ni, but increases for Cu. Metal substitution changes the *c* lattice parameter, which is sensitive to interactions between the mackinawite sheets, as much as it does the *a* and *b* lattice parameters. Upon intercalation, the unit cell volume and *c* parameter increase but the *a* and *b* parameters decrease. Experimental structural data are consistent with our results for metal-substituted FeS. We determined the thermodynamic stability of metal-incorporated FeS by computing the free energy involved in the metal incorporation reactions as a function of chemical potential of sulfur. The thermodynamic results lead to the general conclusions that metal incorporation into mackinawite most likely occurs via substitution, which may be important to influence phase transformation pathways of mackinawite.

INTRODUCTION

Transition-metal-enriched mackinawite (tetragonal FeS) is an exemplar system to gain insight into the effects of metal incorporation on sulfide mineral phase transformations and to understand the formation processes of metal sulfide ore deposits (Blain, 1978; Lennie and Vaughan, 1996; Takeno and Clark, 1967; Zôka et al., 1972; Zavašnik et al., 2014). Structurally, mackinawite comprises edge-sharing sheets of FeS_4 tetrahedra arranged on a tetragonal lattice (*P4/nmm* symmetry, with $a = b = 3.67$ Å, $c = 5.03$ Å) and stacked along the *c* direction, with stabilization through van der Waals (vdW) interactions (Lennie et al., 1995; Rickard et al., 2006). The extant literature suggests that incorporated transition metals can occupy three structurally distinct sites in mackinawite (Figure 1): Fe substitution (Sub) and intercalation between FeS_4 tetrahedral sheets, either at a tetrahedral interstitial site (I-td) or a square-pyramidal interstitial site (I-sp), also described as an "octahedral hole" by Ward (1970).

Vaughan (1969) analyzed the structure of nickelian mackinawite (18.7 wt % Ni) from a nickel ore deposit, reporting lattice parameters slightly smaller [by 0.03 Å along the *c* axis and ≤ 0.006 Å along the *a* (= *b*) axis] than those of pure mackinawite. Clark (1970) inferred from micro-indentation hardness measurements that cobaltian mackinawite (16.5 wt% Co) from a copper-cobalt ore deposit had lattice parameters even smaller than those of nickelian mackinawite. The decreases in unit cell size were attributed by Clark (1970) to substitution of Fe by Co or Ni (i.e., metal incorporation at the Sub site). In response, Vaughan (1970) cautiously proposed that metals could also intercalate between sheets (i.e., incorporation at the I-td or I-sp site). This proposal has been widely cited in the literature (Morse and Rickard, 2004; Muñoz-Santiburcio et al., 2013; Mullet et al., 2002; Watson et al., 1995; Wolthers et al., 2003). Zavašnik et al. (2014) observed a significant increase in the unit cell size (*a* = 3.76

72 Å, c = 5.43 Å) for amorphous FeS nanoparticles reacted with Cu (Cu: Fe ratio ≈ 0.1). They
73 conjectured that Cu intercalates into mackinawite leading to the cell expansion. However, no
74 direct evidence supporting transition metal intercalation has yet been reported.

75 In a systematic approach to examine the structural effects of both substitution and
76 intercalation for three important transition metals, Co, Ni, and Cu, we studied metal-
77 incorporated FeS using density functional theory (DFT). Quantum mechanical geometry-
78 optimization based on DFT with periodic boundary conditions provides reliable and detailed
79 information on solid-phase structures (Milman et al., 2000; Payne et al., 1992) and thus is a
80 useful method to investigate mineral structures for which significant ambiguities exist in the
81 interpretation of experimental data, or where a variety of samples is difficult to obtain for
82 experimental study. Conventional semilocal DFT, such as DFT under the generalized
83 gradient approximation (GGA), does not take weak dispersion forces into account. Therefore,
84 when vdW interactions are a significant component of the total energy of a solid, as they are
85 for mackinawite, the errors in calculating structural parameters can also be significant (e.g.,
86 the c lattice parameter). In our study, we used DFT combined with a tested semi-empirical
87 correction to account for dispersive vdW interactions, the DFT–D method (Grimme, 2006).
88 This method offers both accuracy and a more manageable computational expense than *ab*
89 *initio* wave function methods or quantum Monte Carlo simulations (McNellis et al., 2009;
90 Tunega et al., 2012). We validated the DFT–D approach by successful geometry optimization
91 of $FeSe_{1-x}S_x$ (anion-substituted FeSe), $Fe_{1-x}Me_xSe$ (Me = Co, Ni, and Cu (cation-substituted
92 FeSe), and $FeNi_{0.125}Te$ (Ni-intercalated FeTe), the structures of which are relatively well
93 characterized by experiment. Both FeSe and FeTe are iron chalcogenides that share
94 structural, electronic, and magnetic properties with FeS (Kwon et al., 2011; Lennie et al.,

1995; Mizuguchi and Takano, 2010). For a range of incorporated metal content, we examined how the structure of FeS changes when a metal is substituted at the Fe site or intercalated into the FeS interlayer. Specifically, we examined the structural effects of metal incorporation for $Fe_{1-x}Me_xS$ (metal-substituted FeS) and $FeMe_xS$ (metal-intercalated FeS, I-td or I-sp site), where Me = Co, Ni, Cu and $0 \leq x \leq 0.25$. Formation energies of the metal-incorporated FeS were compared to determine which incorporation process is a most favorable for a given transition metal.

COMPUTATIONAL DETAILS

The initial structures of transition-metal incorporated FeSe and FeS were created based on geometry optimized FeSe and FeS unit cells. For substitution calculations, one Fe in an FeSe or FeS supercell was replaced by a transition metal (Me) to give $Fe_{1-x}Me_xSe$ or $Fe_{1-x}Me_xS$, with the mole fraction x in the range $0.0625 \leq x \leq 0.25$. The structural formulas were specifically: $Fe_{15}Me(Se, S)_{16}$ (x = 0.0625), $Fe_7Me(Se, S)_8$ (x = 0.125) and $Fe_3Me(Se, S)_4$ (x = 0.25), where Me is Co, Ni, or Cu. For intercalation calculations ($FeMe_xSe$ or $FeMe_xS$), the structural formulas were: $Fe_{16}Me(Se, S)_{16}$ (x = 0.0625), $Fe_8Me(Se, S)_8$ (x = 0.125), and $Fe_4Me(Se, S)_4$ (x = 0.25).

All DFT calculations were carried out using the CASTEP code (Clark et al., 2005) which implements DFT with periodic boundaries and a planewave basis set. We used ultrasoft pseudopotentials (Vanderbilt, 1990) to describe the strong Coulomb potentials between atomic nuclei and core electrons. Our Fe pseudopotential treats both 3*s* and 3*p* states as the valence state, with the valence electron configuration being $3s^2 3p^6 3d^6 4s^{1.75}$ because Fe pseudopotentials treating 3*p* states as core electrons do not adequately reproduce the magnetic ground state ordering energetics of many layer-type Fe chalcogenides or pnictides

(Kwon et al., 2011; Mazin et al., 2008). The valence electron configurations for the S, Se, and Te pseudopotentials are $3s^2 3p^4$, $4s^2 4p^4$, and $5s^2 5p^4$, respectively, while the Co, Ni, and Cu pseudopotentials have $3d^7 4s^{1.95} 4p^{0.05}$, $3d^8 4s^2$, and $3d^7 4s^{0.5} 4p^{0.001}$ valence electron configurations, respectively. All calculations were performed under the spin-polarized general gradient approximation for electron correlation using the Perdew, Burke and Ernzerhof functional (Perdew et al., 1996). Because of the metallic character of these materials, the GGA+U method is not required to describe itinerant *d* electrons (Ferber et al., 2010) and, therefore, no Hubbard U was used in our calculations.

In the DFT–D approach, the total energy (E_{tot}) is calculated by addition of an interatomic pairwise C_6R^{-6} term to the DFT energy (E_{DFT}):

$$E_{tot} = E_{DFT} - \frac{1}{2}\sum_{A,B} f_{damp}\left(R_{A,B}, R_A^0, R_B^0\right) C_{6AB} R_{AB}^{-6},$$

where R_{AB} is the separation between atoms *A* and *B*, C_{6AB} is the corresponding C_6 coefficient, and R^0_A and R^0_B are vdW radii (Grimme, 2011). The interaction is damped at short range by the f_{damp} function. The C_{6AB} parameters can be obtained either by DFT calculations of atomic ionization potentials and dipole polarizabilities using the London formula for dispersion [the G06 scheme (Grimme, 2006)] or by time-dependent DFT calculations using the electronic-density-based atomic volume for each atom [the TS scheme (Tkatchenko and Scheffler, 2009)]. We used the G06 scheme for all calculations.

A planewave basis set was expanded to a kinetic energy cutoff of 400 eV. The cutoff energy for the augmentation-charge density was set to 1600 eV in geometry optimizations and 6400 eV in phonon calculations. The primitive Brillouin zone was sampled with a 14 × 14 × 11 point grid in *k* space (Monkhorst and Pack, 1976) for FeS or FeSe unit cells, and

Gaussian broadening of 0.01 eV was applied to partially-occupied bands. Proportionally reduced grids were used for supercells. Using this selection of the energy cutoffs and k -point grid, the atomic force converged to within 0.01 eV/Å and the total energy converged to within 0.0001 eV. The precision of our geometry optimization method was estimated to be significantly better than 0.001 Å for the a parameter and 0.005 Å for the c parameter of transition-metal-incorporated iron chalcogenides. Magnetic ordering among Fe moments was checkerboard antiferromagnetic in the sheet (i.e., each Fe was surrounded by Fe having opposite spin), with the initial magnetic moment of the transition metal being in the same direction as the Fe that was being substituted. [See Kwon et al. (2011) for details concerning Fe magnetic ordering.] The Broyden-Fletcher-Goldfarb-Shanno (BFGS) procedure was followed in the geometry optimizations with correction for any finite basis set error (Francis and Payne, 1990). The residual atomic force was less than 0.01 eV/ Å, and the root-mean-square stress was less than 0.02 GPa.

The relative stability of metal-incorporated FeS was determined by comparison of the formation energies involved in the following reactions:

$$(1\text{-}x)\ \mathrm{FeS} + x\ \mathrm{MeS} = \mathrm{Fe}_{(1-x)}\ \mathrm{Me}_x\mathrm{S}\ \text{(substitution)}$$

$$\mathrm{FeS} + x\ \mathrm{MeS} = \mathrm{FeMe}_x\mathrm{S} + x/2\ \mathrm{S}_{2(g)}\ \text{(intercalation)},$$

where x is the mole fraction of Me, which represents Co, Ni, or Cu: FeS = mackinawite; CoS = NiAs-type CoS (jaipurite); NiS = NiAs-type NiS; CuS = covellite. As the reference solid phases, we used metal monosulfides (MeS) rather than elemental metals to minimize incomplete error cancellation in the total energy differences between chemically dissimilar phases (Lany, 2008). Takeno et al. (1982) synthesized transition-metal incorporated mackinawite by using multiple metal sulfides at high temperature. The formation energy (ΔE^f) for metal substituted (Sub) or intercalated (INT) FeS was calculated as:

$$\Delta E^{f}_{Sub} = F^{phon}_{Sub} - (1-x)F^{phon}_{FeS} - xF^{phon}_{MeS}$$

$$\Delta E^{f}_{INT} = F^{phon}_{INT} - F^{phon}_{FeS} - xF^{phon}_{MeS} + x\mu_S,$$

where $F^{phon}(T)$ is the Helmholtz free energy, and $\mu_S(T,p)$ is the chemical potential of sulfur gas. The relevance of $F^{phon}(T)$ derives from the fact that phase relationships of sulfides found at the typical depths of ore deposits are relatively insensitive to pressure, and so are mostly used as geothermometers (Barton, 1970). Natural mackinawite commonly occurs in contact metasomatic, pneumatolytic, and hydrothermal deposits within metamorphic rocks and ultramafic rocks (Zôka et al., 1972, and references cited therein); thus we calculated ΔE^f at temperatures up to 1000 K.

The Helmholtz free energy of a metal sulfide was taken as:

$$F^{phon} = E_{tot} + F_{vib} + E_{conf},$$

where E_{tot} is the total energy at 0 K, F_{vib} is the purely vibrational contribution (i.e., zero point energy, vibrational energy, vibrational entropy) at temperature T, and E_{conf} is the configurational entropy contribution for metal-incorporated FeS. The value of E_{conf} was calculated under the assumption of ideal mixing: for $Fe_{1-x}Me_xS$, $E_{conf} = k_BT\,[(1-x)\ln(1-x) + x\ln x]$, where k_B is the Boltzmann constant; for $FeMe_xS$ (I-td), in which Me occupies one I-td interstitial site instead of I-sp site per formula unit, $E_{conf} = -k_BT\ln 2$. The difference between Sub and INT in the $(E_{tot} + F_{vib})$ contribution to ΔE^f was approximately 0.2 – 0.3 eV/f.u. at 1000 K, but the contribution of E_{conf} was only about 0.03 – 0.06 eV/f.u. at 1000 K.

The vibrational contribution (F_{vib}) was calculated as the harmonic phonon density of states. We performed the phonon calculations using the usual finite displacement method, constructing supercells of a geometry-optimized unit cell to obtain dynamical matrix at

different phonon wavevectors (Ackland et al., 1997; Parlinski et al., 1997). In a supercell, each nonequivalent atom was displaced by ± 0.005 Å along the Cartesian directions and the forces on all atoms of the supercell perturbed by the atom displacement were calculated within a real space of at least 6.5 Å radius. The Fourier transform of the force constant matrix produces the dynamical matrix, whose eigenvalues (phonon frequencies) were integrated over the Brillouin zone to compute thermodynamic quantities, such as enthalpy and vibrational entropy, at different temperatures (Dove, 1993). For FeS, CoS, and NiS, the supercell size was 4 × 4 × 3 (96 atoms). The supercell size for CuS, body centered cubic ferromagnetic Fe, and orthorhombic S was 4 × 4 × 1 (96 atoms), 5 × 5 × 5 (250 atoms), and 2 × 1 × 1 (256 atoms), respectively. For metal-incorporated FeS, supercells with checkerboard antiferromagnetic ordering contained 192 or 216 atoms for Sub and 204 or 243 atoms for INT.

An H_2S + H_2 gas mixture is often used to control the fugacity of sulfur gas (Sack and Ebel, 2006). We inferred $\mu_S(T,p)$, which depends on the partial pressure ratio of H_2S and H_2, under the assumption of ideal gas behavior at equilibrium with a metal sulfide (Bollinger et al., 2003; Raybaud et al., 2000):

$$\mu_S(T,p) = \mu_{H_2S}(T,p) - \mu_{H_2}(T,p)$$

$$= \left[h_{H_2S}(T,p^0) - h_{H_2}(T,p^0)\right] - T[s_{H_2S}(T,p^0) - s_{H_2}(T,p^0)] + k_B T \ln(\frac{p_{H_2S}}{p_{H_2}})$$

$$= \left[\Delta h_{H_2S}(T,p^0) - \Delta h_{H_2}(T,p^0)\right] + \left[ZPE_{H_2S} - ZPE_{H_2}\right] + (E_{H_2S} - E_{H_2}) -$$

$$T[s_{H_2S}(T,p^0) - s_{H_2}(T,p^0)] + k_B T \ln(\frac{p_{H_2S}}{p_{H_2}}),$$

where *h*, *s*, *ZPE, and E* are the enthalpy, entropy, zero point energy, and internal energy of $H_2S_{(g)}$ or $H_{2(g)}$, respectively, and *p* is a partial pressure (p^0 = 1 atm). The values of $\Delta h(T, p^0)$

and $s(T, p^0)$ can be found in standard thermodynamic tables (e.g., http://webboook.nist.gov and http://cccbdb.nist.gov). The difference in ZPE or E was calculated using a 18 × 18 × 18 Å simulation box containing a single H_2S or H_2 molecule.

Comparison of formation energies is meaningful only when the chemical potential varies within a bounded range (Alfonso, 2010; Krishnamoorthy et al., 2013; Reuter and Scheffler, 2001). The upper limit of the allowed range can be set by the chemical potential of sulfur in the solid orthorhombic state (μ_S^0). For sulfur to be stable in a metal sulfide at equilibrium, μ_S must be smaller than μ_S^0 (i.e., $\mu_S - \mu_S^0 \leq 0$). The lower limit of the allowed range was determined by considering:

$$\Delta E_{FeS}^f = g_{FeS} - \mu_{Fe}^0 - \mu_S^0$$

$$= (\mu_{Fe} + \mu_S) - \mu_{Fe}^0 - \mu_S^0$$

$$= (\mu_{Fe} - \mu_{Fe}^0) + (\mu_S - \mu_S^0),$$

where ΔE_{FeS}^f, g_{FeS}, μ_{Fe}^0 is the formation energy of FeS, the free energy of FeS, and the chemical potential of elemental Fe, respectively. The value of μ_{Fe} should be smaller than μ_{Fe}^0 (i.e., $\mu_{Fe} - \mu_{Fe}^0 \leq 0$). This condition leads to: $\mu_S - \mu_S^0 = \Delta E_{FeS}^f - (\mu_{Fe} - \mu_{Fe}^0) \geq \Delta E_{FeS}^f$. We used ΔE_{FeS}^f = – 0.68 eV computed at 0 K with reference to elemental Fe and orthorhombic elemental S. Therefore, the allowed range of μ_S was – 0.68 eV < $\Delta\mu_S = \mu_S - \mu_S^0$ < 0 eV.

RESULTS AND DISCUSSION

Validation of the DFT–D method

The total energy of FeS or FeSe is compared between the DFT and the DFT–D methods in Figure 2. Without vdW dispersion corrections, a very shallow energy minimum

232 results along with an estimated *c* parameter which is very different from the experimental
233 value, whereas the *c* parameter calculated using DFT–D agrees very well with experimental
234 data. Fully geometry-optimized structural results are summarized in Table 1. Both
235 antiferromagnetic (AFM) ordering among Fe spins and the non-magnetic (NM) state were
236 examined, but we found that AFM ordering is more stable than the NM state for both FeS and
237 FeSe (Kwon et al., 2011; Subedi et al., 2008). The Fe moments we calculated for FeS and
238 FeSe were larger than experimental values, which is a common shortcoming of DFT for
239 metallic layer type Fe chalcogenides and pnictides (Mazin and Johannes, 2009). The
240 structural parameters (i.e., lattice parameters, bond distances, and S or Se coordinate) of the
241 AFM state differed from experiment by < 1.5 % for FeS and by < 0.5 % for FeSe, whereas
242 those of the NM state differed by < 3.8 % for FeS and 3.5 % for FeSe. Given these
243 comparisons, all subsequent results described herein are based on AFM ordering.

244 The lattice parameters of $FeSe_{1-x}S_x$ calculated using DFT–D (Fig. 3) are in excellent
245 agreement with experimental data (Mizuguchi et al., 2009), although the *c* parameter is
246 slightly underestimated when the S content is large. Our DFT–D calculations also were able
247 to reproduce two experimentally observed trends: as the S content increases in FeSe, both
248 lattice parameters decrease, with the change in *c* being larger than that in *a* (=*b*). The
249 experimentally determined *c* parameter at $x = 0.5$ was larger than at $x = 0.4$, and thus the
250 decrease of *c* was not linear as a function of *x* (S content). Our calculations did not show an
251 increase in *c* at $x = 0.5$, but the decreasing gradient of *c* varied slightly depending on whether
252 *x* was smaller or larger than 0.5. Experimental data are not shown for $0.5 < x < 1.0$ in Figure
253 3 because only limited solid solution appears to occur between FeSe and FeS (Finck et al.,

2012; Mizuguchi et al., 2009). We estimated the excess heats of $FeSe_{1-x}S_x$ formation with respect to pure FeS and FeSe (ΔE_{ex}) from the expression:

$$\Delta E_{ex} = E\ (FeSe_{1-x}S_x) - (1-x)E(FeSe) - xE(FeS)$$

where E on the right side is, respectively, the total energy of $FeSe_{1-x}S_x$, FeSe, and FeS. The ΔE_{ex} value for $FeSe_{1-x}S_x$ was nearly zero (+ 2 to about + 6 meV/formula unit) for all compositions examined. Thus the existence of $FeSe_{1-x}S_x$ in the range $0.5 < x < 1.0$ cannot be ruled out based on energy considerations alone.

The effects of transition metal substitution on the structure of FeSe are more complicated than those of anion substitution. As substitution increases, *c* tends to decrease; however, *a* either increases or decreases depending the substituting metal, as shown in Figure 4. Specifically, the decrease of *c* in the case of substitution by Cu is larger than that in the case of Co or Ni; furthermore, the increase of *a* in the case of Ni is small compared to that for Cu substitution. These experimental trends for FeSe were well reproduced in our DFT–D calculations (see the solid circles in Fig. 4), although the calculated *c* parameter for $Fe_{1-x}Ni_xSe$ was in poor agreement with experimental data. Figure 4 also shows that metal substitution within a $FeSe_4$ tetrahedral sheet affects not only the *a* parameter significantly, but also the *c* parameter, indicating that metals other than Fe that bind to Se can strongly affect the vdW forces between the sheets.

As the metal content increases, the *a* parameter decreases in the case of Co substitution, but increases in the case of Cu. In the case of Ni substitution, the lattice parameter increases very slightly as the Ni fraction varies (Fig. 4). The decrease in the lattice parameters of $FeSe_{1-x}S_x$ with increasing *x* can be understood by considering the smaller size of S relative to Se; but, for $Fe_{1-x}Me_xSe$, comparisons of cation size alone cannot explain the

trends in variation of the lattice parameters. The ionic radius of Co^{2+} is 0.58 Å, that of Ni^{2+} is 0.55 Å, and that of Cu^{2+} is 0.57 Å (Shannon, 1976), all of which are smaller than that of Fe^{2+} (0.63 Å) and so do not explain their differing structural effects. The larger metallic radius (Wells, 1991) of Cu relative to Fe (1.28 vs. 1.26 Å) may explain the increase of *a* for $Fe_{1-x}Cu_xSe$ (Vaughan, 1970), but the smaller metallic radius of Ni relative to Fe (1.24 vs. 1.26 Å) cannot account for the increase in *a* following substitution by Ni. Thus structural trends in metal-substituted FeSe cannot be predicted by crystal chemical effects alone but require a quantitative model of bonding energetics as provided by electronic structure calculations.

We further tested our method by examining the structure of $FeNi_xTe$, which is a layer type Fe chalcogenide in which the interstitial sites for Ni in the interlayer are well characterized. According to a single-crystal refinement of $FeNi_{0.1}Te$ by Zajdel et al. (2010), Ni is located at the I-sp site rather than the I-td site. Our DFT–D calculations for $FeNi_{0.125}Te$ showed that the I-sp site is indeed energetically more favorable than the I-td site (see Table 2). The structural parameters also were in better agreement with experimental data when Ni was placed at the I-sp site. The *c* lattice parameter and Z_{Ni} for $FeNi_{0.125}Te$ we calculated differed from the experimental data by less than 0.2 %.

Transition metal substitution in FeS

The trend of changes in the lattice parameters of FeS following metal substitution is similar to those for FeSe, except for the case of Cu, as shown in Figure 5. The *c* parameter of $Fe_{1-x}Cu_xS$ increases with *x*, whereas that of $Fe_{1-x}Cu_xSe$ decreases with *x* (compare Fig. 4c and Fig. 5c). These opposing trends imply that doping the same transition metal exerts opposite pressures on the structure depending on the chalcogenide: substitution of Cu compresses the sheet structure of FeSe along the *c*-axis, but expands the FeS sheet structure. We also

300 examined the interlayer spacing (*h,* the height difference of S or Se) between neighboring
301 sheets and the thickness (*t*) of a single tetrahedral sheet for FeSe and FeS. In $Fe_{1-x}Cu_xSe$, the
302 decrease in *c* with increasing *x* resulted from a reduction in *h* rather than *t*. For example, in
303 the case of $Fe_{0.75}Cu_{0.25}Se$, *h* and *t* decreased by 0.06 Å and 0.02 Å, respectively, as compared
304 to pure FeSe. However, the increase in *c* for $Fe_{1-x}Cu_xS$ we attribute to an increase in the sheet
305 thickness (*t*). In $Fe_{0.75}Cu_{0.25}S$, *h* and *t* increased by less than 0.01Å and by 0.06 Å,
306 respectively, as compared to FeS.

307 When Co occupies the Fe site, the unit cell volume of $Fe_{1-x}Co_xS$ monotonically
308 decreases as a function of *x* (Fig. 5a), which is consistent with the observed monotonic
309 increase of the Vickers micro-indentation hardness as a function of the Co content in FeS
310 (Clark, 1970), where it was assumed that Co substitutes for Fe and the reduction in volume
311 can be attributed to the monotonic decrease in *a* as a function of Co content. However, we
312 found that the *c* parameter did not decrease monotonically: initially it increased slightly with
313 increasing *x* and then decreased when $x > 0.125$. By contrast, the volume of $Fe_{1-x}Cu_xS$
314 increases as a function of *x* because of the increase in both *a* and *c*, which is consistent with
315 experimental observations for Cu-reacted amorphous FeS nanoparticles (Zavašnik et al.,
316 2014).

317 In the case of substitution by Ni, the volume of the FeS unit cell remains nearly
318 constant as a function of *x*, changing by less than 1% (Fig. 5a). This is a result of opposing
319 trends in the variations of lattice parameters, with a greater change in *c* than in *a*. As *x*
320 increases, *a* increases, but *c* decreases (a slight exception occurs at $x = 0.0625$). In
321 $Fe_{0.75}Ni_{0.25}S$, the *a* parameter increased by 0.027 Å as compared with FeS, but *c* decreased by

322 0.078 Å. Vaughan (1969) also reported a much larger change in *c* (0.03 Å) than in *a* (0.006
323 Å) for nickelian mackinawite as compared with pure FeS.

324 **Transition metal intercalation into FeS**

325 Significant expansion in the *c* parameter occurs following transition metal
326 intercalation into the FeS interlayer, the effect being greatest with Cu and least with Ni (Fig.
327 6). For substitution, the change in the *a* parameter was always greater than or comparable to
328 the change in the *c* parameter; but, for intercalation, the latter was considerably larger than
329 the former. This trend can be characterized by the ratio *c/a*: substitution results in a smaller
330 *c/a* ratio than intercalation. The *c/a* ratio for pure FeS was calculated as 1.35, slightly smaller
331 than the experimental value, 5.03/3.67 = 1.37. The calculated *c/a* ratio was 1.36 for
332 $Fe_{0.75}Co_{0.25}S$ (substitution), and it was 1.37 (I-td site) or 1.45 (I-sp site) for $FeCo_{0.25}S$
333 (intercalation). For $Fe_{0.75}Ni_{0.25}S$ the calculated ratio was 1.32, and for $FeNi_{0.25}S$ it was 1.39 (I-
334 td site) or 1.46 (I-sp site). As in the Co and Ni cases, our calculated *c/a* ratio for Cu
335 substitution was lower than the ratio for Cu intercalation: 1.34 for $Fe_{0.75}Cu_{0.25}S$ and 1.43 (I-td
336 site) or 1.47 (I-sp site) for $FeCu_{0.25}S$.

337 When a transition metal occupied the I-td site, the *a* parameter changed by less than
338 0.01 Å as compared with pure FeS (Fig. 6a). However, when the metal occupied the I-sp site,
339 this lattice parameter decreased by as much as 0.09 Å (Fig. 6b). In the case of Co, the effect
340 of intercalation at the I-sp site was as large as the effect of substitution (compare Fig. 5b with
341 Fig. 6b). Because of this significant decrease in the *a* parameter, the volume of the I-sp-
342 intercalated FeS was comparable to that of I-td-intercalated FeS, despite the much greater *c*
343 parameter. Intercalation at the I-sp site places the metal just below an apical S, but with a
344 slightly larger *z*-coordinate, by 0.4 – 0.6 Å, than the four S of the neighboring FeS sheet (see

Fig. 1), resulting in a shorter distance to the apical S than for the other four S. For example, at the I-sp site in $FeCu_{0.125}S$, the distance between Cu and the apical S, *d*(Cu-S), was 2.14 Å, while *d*(Cu-S) was 2.68 Å for the other four S. For the I-td site, we found *d*(Cu-S) = 2.30 Å, which is similar to the same interatomic distance in chalcopyrite. The presence of a five-coordinated metal in the interlayer also resulted in a decrease in the Fe-Fe separation within the FeS sheet. In $FeCu_{0.125}S$, the average Fe–Fe separation was reduced from 2.61 Å in pure FeS to 2.58 Å in intercalated FeS.

Deducing incorporation mechanisms

Our formation energy calculations indicate that substitution is a favorable mechanism when metals incorporate into mackinawite. The formation energy (ΔE^f) of $FeMe_xS$ (I-td) varied linearly as a function of S chemical potential (μ_S), while ΔE^f of $Fe_{1-x}Me_xS$ (Sub) was independent of μ_S (Fig. 7). [In calculating ΔE^f for intercalation, only the I-td site was considered because, in contrast to $FeNi_{0.125}Te$ (Table 2), this site was more stable than the I-sp site in FeS by 50 – 360 meV/f.u., depending on metal type and content.] We found that Sub is thermodynamically more stable than I-td for all three metals within the allowed range of μ_S (–0.68 eV < $\Delta\mu_S = \mu_S - \mu_S^0$ < 0 eV). As the metal fraction increases, the stability of Sub is further enhanced, while the stability of I-td diminishes: the formation energy of Sub is more negative and of I-td, more positive. Increasing the temperature results in similar trends, but not as pronounced. The $p(H_2S)/p(H_2)$ scales shown in Figure 7c further indicate that, at high $p(H_2S)/p(H_2)$ (i.e., sulfidic environment), substitution is by far the more favorable mechanism of metal incorporation.

For Co or Ni incorporation, the thermodynamic stability of substitution over intercalation also agrees well with structural data, which shows that the *c* parameter for

368 cobaltian or nickelian mackinawite is smaller than that for pure FeS (Clark, 1970; Vaughan,
369 1969). Our computations show that the *c* parameter of FeS decreases following Co or Ni
370 substitution; however, intercalation led to a considerable increase in the *c* parameter. While
371 Co and Ni share the trends in structural changes upon metal incorporation, the temperature
372 dependence of relative stability differs between the metals. As temperature increases from
373 300 K to 900 K, the value of ΔE^f for Co-Sub remains nearly constant or becomes slightly less
374 negative (Fig. 7a and d), but that for Ni-Sub becomes noticeably more negative (Fig. 7b and
375 e). This different thermodynamic behavior is due to the difference in the vibrational
376 contribution to ΔE^f (ΔF_{vib}) between the two metals. For $Fe_{0.75}Co_{0.25}S$, ΔF_{vib} increases with
377 temperature ($\approx$ +50 meV/f.u. at 900 K) comparably to the configurational entropy
378 contribution (E_{conf}, $\approx$ –40 meV/f.u. at 900 K). For $Fe_{0.75}Ni_{0.25}S$, however, ΔF_{vib} is negligible
379 (< –10 meV/f.u. at 900 K) while E_{conf} is $\approx$ –40 meV/f.u. at 900 K.

380 Although ΔE^f for $FeCu_{0.125}S$ is similar to that for $Fe_{0.875}Cu_{0.125}S$ near the lower limit
381 of μ_S (Fig. 7c), which corresponds to low $p(H_2S)/p(H_2)$ (i.e., highly reducing environment),
382 in general, Sub is more stable than I-td for Cu incorporation. This greater stability of Sub
383 over I-td is also consistent with structural data. For Cu-reacted FeS nanoparticles, both *a* and
384 *c* are larger than for pure FeS (Zavašnik et al., 2014). This increase in the lattice parameters
385 with Cu incorporation matches only our Cu-sub trends (Fig. 5b and c) and Figure 6 shows
386 that the parameter *a* tends to decrease when Cu is intercalated at either the I-td or I-sp site.

387 Metal incorporation has been postulated to increase the stability of mackinawite
388 (Takeno and Clark, 1967; Zavašnik et al., 2014). Our finding of a negative ΔE^f of Co-Sub and
389 Ni-Sub supports this hypothesis, and shows further that the mechanism is substitution, not
390 intercalation. These results also explain why, in the absence of water, it is easier to synthesize

391 metal-incorporated mackinawite than the pure mineral (Takeno et al., 1982). On the other
392 hand, Cu-sub shows a negative ΔE_f only above 770 K, when x = 0.125, or above 510 K, when
393 x = 0125, and it is generally less negative than for Co- or Ni-sub. Thus we would predict that
394 mackinawite may accommodate a smaller content of Cu than Co or Ni. Indeed, in natural
395 mackinawite, the Cu content is typically < 10 wt %, whereas the Co or Ni content is typically
396 < 20 wt % (Clark, 1970; Clark and Clark, 1968; Vaughan, 1969; Zôka et al., 1972).

397 ## IMPLICATIONS

398 Naturally occurring mackinawite typically contains several species of transition metal.
399 This study is the first to examine systematically the relationships among chemical
400 composition, structure, and thermodynamic stability of transition-metal-incorporated
401 mackinawite. Our results show that transition metals tend to incorporate into mackinawite by
402 substitution at the Fe sites within the FeS_4 tetrahedral sheets accompanied by changes in bond
403 distances. Metal substitution enhances the stability of mackinawite to a degree which depends
404 on both the metal and temperature. In materials processing, iron sulfides are used as catalysts
405 and the catalytic activity is often controlled by doping with transition metals. Thus our
406 findings not only help to understand the transformations of transition-metal-incorporated
407 mackinawite into various metal sulfides in ore deposits, but may also suggest synthetic routes
408 for developing enhanced metal-sulfide catalysts.

409 ## ACKNOWLEDGMENTS

410 This research was supported by the Basic Science Research Program through the
411 National Research Foundation of Korea (NRF) funded by the Ministry of Science, ICT and
412 Future Planning (NRF-2013R1A1A1004657) and a 2012 Research Grant from Kangwon
413 National University. Support for this research also was received from the University of

California at Berkeley through the appointment of the third author as a Chancellor's Professor. Computations were performed by using resources of the National Energy Research Scientific Computing Center, which is supported by the Office of Science of the U.S. Department of Energy under Contract No. DE-AC02-05CH11231.

REFERENCES CITED

Ackland, G.J., Warren, M.C., and Clark, S.J. (1997) Practical methods in ab initio lattice dynamics. Journal of Physics: Condensed Matter, 9, 7861-7872.

Alfonso, D.R. (2010) Computational investigation of FeS_2 surfaces and prediction of effects of sulfur environment on stabilities. Journal of Physical Chemistry C, 114, 8971-8980.

Barton, P.B. (1970) Sulfide Petrology. In P.H. Ribbe, Ed. Mineralogical Society of America Special Paper, 3, p. 187-198. Mineralogical Society of America.

Blain, C.F. (1978) Hydrothermal nickelian mackinawite in nickel mineralization at Wadi Qatan, Saudi Arabia. Mineralogical Magazine, 42, 284-286.

Bollinger, M.V., Jacobsen, K.W., and Nørskov, J.K. (2003) Atomic and electronic structure of MoS_2 nanoparticles. Physical Review B, 67, 085410.

Clark, A.H. (1970) Nickelian mackinawite from Vlakfontein, Transvaal: a discussion. American Mineralogist, 55, 1802-1807.

Clark, A.H., and Clark, A.M. (1968) Electron microprobe analysis of mackinawite from the Ylöjärvi deposit, Finland. Neues Jahrbuch Fur Mineralogie-Monatshefte, 6, 259-268.

Clark, S.J., Segall, M.D., Pickard, C.J., Hasnip, P.J., Probert, M.J., Refson, K., and Payne, M.C. (2005) First principles methods using CASTEP. Zeitschrift Fur Kristallographie, 220, 567-570.

438 Dove, M.T. (1993) Introduction to Lattice Dynamics. Cambridge University Press.
439 Ferber, J., Zhang, Y.Z., Jeschke, H.O. and Valentí, R. (2010) Analysis of spin-density wave
440 conductivity spectra of iron pnictides in the framework of density functional theory.
441 Physical Review B, 82, 165102.
442 Finck, N., Dardenne, K., Bosbach, D., and Geckeis, H. (2012) Selenide retention by
443 mackinawite. Environmental Science & Technology, 46, 10004-10011.
444 Francis, G.P., and Payne, M.C. (1990) Finite basis set corrections to total energy
445 pseudopotential calculations. Journal of Physics-Condensed Matter, 2, 4395-4404.
446 Grimme, S. (2006) Semiempirical GGA-type density functional constructed with a long-
447 range dispersion correction. Journal of Computational Chemistry, 27, 1787-1799.
448 Grimme, S. (2011) Density functional theory with London dispersion corrections. WIREs
449 Computational Molecular Science, 1, 211-228.
450 Krishnamoorthy, A., Herbert, F.W., Yip, S., Van Vliet, K.J., and Yildiz, B. (2013) Electronic
451 states of intrinsic surface and bulk vacancies in FeS_2. Journal of Physics-Condensed
452 Matter, 25, 045004.
453 Kwon, K.D., Refson, K., Bone, S., Qiao, R., Yang, W.-l., Liu, Z., and Sposito, G. (2011)
454 Magnetic ordering in tetragonal FeS: Evidence for strong itinerant spin fluctuations.
455 Physical Review B 83, 064402.
456 Lany, S. (2008) Semiconductor thermochemistry in density functional calculations. Physical
457 Review B, 78, 245207.
458 Lennie, A.R., Redfern, S.A.T., Schofield, P.F., and Vaughan, D.J. (1995) Synthesis and
459 Rietveld crystal structure refinement of mackinawite, tetragonal FeS. Mineralogical
460 Magazine, 59, 677-683.

461 Lennie, A.R., and Vaughan, D.J. (1996) Spectroscopic studies of iron sulfide formation and
462 phase relations at low temperatures. In M.D. Dyar, C. McCammon, and M.W.
463 Schaefer, Eds. Mineral Spectroscopy: A Tribute to Roger G. Burns, p. 117-132. The
464 Geochemical Society, Houston.
465 Mazin, I.I., and Johannes, M.D. (2009) A key role for unusual spin dynamics in
466 ferropnictides. Nature Physics, 5, 141-145.
467 Mazin, I.I., Johannes, M.D., Boeri, L., Koepernik, K., and Singh, D.J. (2008) Problems with
468 reconciling density functional theory calculations with experiment in ferropnictides.
469 Physical Review B, 78, 085104.
470 McNellis, E.R., Meyer, J., and Reuter, K. (2009) Azobenzene at coinage metal surfaces: Role
471 of dispersive van der Waals interactions. Physical Review B, 80, 205414.
472 Milman, V., Winkler, B., White, J.A., Pickard, C.J., Payne, M.C., Akhmatskaya, E.V., and
473 Nobes, R.H. (2000) Electronic structure, properties, and phase stability of inorganic
474 crystals: A pseudopotential plane-wave study. International Journal of Quantum
475 Chemistry, 77, 895-910.
476 Mizuguchi, Y., and Takano, Y. (2010) Review of Fe Chalcogenides as the Simplest Fe-Based
477 Superconductor. Journal of the Physical Society of Japan, 79, 102001.
478 Mizuguchi, Y., Tomioka, F., Tsuda, S., Yamaguchi, T., and Takano, Y. (2009) Substitution
479 effects on FeSe superconductor. Journal of the Physical Society of Japan, 78, 074712.
480 Monkhorst, H.J., and Pack, J.D. (1976) Special points for Brillouin-zone integrations.
481 Physical Review B, 13, 5188-5192.
482 Morse, J.W., and Rickard, D. (2004) Chemical dynamics of sedimentary acid volatile sulfide.
483 Environmental Science & Technology, 38, 131A-136A, 2004.

Muñoz-Santiburcio, D., Wittekindt, C., and Marx, D. (2013) Nanoconfinement effects on hydrated excess protons in layered materials. Nature Communications, 4, 2349.

Mullet, M., Boursiquot, S., Abdelmoula, M., Genin, J.M., and Ehrhardt, J.J. (2002) Surface chemistry and structural properties of mackinawite prepared by reaction of sulfide ions with metallic iron. Geochimica Et Cosmochimica Acta, 66, 829-836.

Parlinski, K., Li, Z.Q., and Kawazoe, Y. (1997) First-Principles Determination of the Soft Mode in Cubic ZrO_2. Physical Review Letters, 78, 4063-4066.

Payne, M.C., Teter, M.P., Allan, D.C., Arias, T.A., and Joannopoulos, J.D. (1992) Iterative minimization techniques for *ab initio* total-energy calculations: molecular-dynamics and conjugate gradients. Reviews of Modern Physics, 64, 1045-1097.

Perdew, J.P., Burke, K., and Ernzerhof, M. (1996) Generalized gradient approximation made simple. Physical Review Letters, 77, 3865-3868.

Raybaud, P., Hafner, J., Kresse, G., Kasztelan, S., and Toulhoat, H. (2000) Ab initio study of the H_2–H_2S/MoS_2 gas–solid interface: The nature of the catalytically active sites. Journal of Catalysis, 189, 129-146.

Reuter, K., and Scheffler, M. (2001) Composition, structure, and stability of RuO_2 (110) as a function of oxygen pressure. Physical Review B, 65, 035406.

Rickard, D., Griffith, A., Oldroyd, A., Butler, I.B., Lopez-Capel, E., Manning, D.A.C., and Apperley, D.C. (2006) The composition of nanoparticulate mackinawite, tetragonal iron(II) monosulfide. Chemical Geology, 235, 286-298.

Sack, R.O., and Ebel, D.S. (2006) Theromochemistry of sulfide mineral solutions. In D. Vaughan, Ed. Reivews in Mineralogy and Geochemistry, 61, p. 265-364. Mineralogical Society of America, Chantilly, Virginia.

Subedi, A., Zhang, L.J., Singh, D.J., and Du, M.H. (2008) Density functional study of FeS, FeSe, and FeTe: Electronic structure, magnetism, phonons, and superconductivity. Physical Review B, 78, 134514.

Takeno, S., and Clark, A.H. (1967) Observations on tetragonal (Fe, Ni, Co)$_{1+x}$S, mackinawite. Journal of Science Hiroshima University, Series C, 5, 287-293.

Takeno, S., Moh, G.H., and Wang, N. (1982) Dry mackinawite synthesis. Neues Jahrbuch Fur Mineralogie-Abhandlungen, 144, 291-342.

Thomas, E.L., Wong-Ng, W., Phelan, D., and Millican, J.N. (2009) Thermopower of Co-doped FeSe. Journal of Applied Physics, 105, 073906.

Tkatchenko, A., and Scheffler, M. (2009) Accurate molecular van der waals interactions from ground-state electron density and free-atom reference data. Physical Review Letters, 102, 073005.

Tunega, D., Bucko, T., and Zaoui, A. (2012) Assessment of ten DFT methods in predicting structures of sheet silicates: Importance of dispersion corrections. Journal of Chemical Physics, 137, 114105.

Vanderbilt, D. (1990) Soft self-consistent pseudopotentials in a generalized eigenvalue formalism. Physical Review B, 41, 7892-7895.

Vaughan, D.J. (1969) Nickelian mackinawite from Vlakfontein, Transvaal. American Mineralogist, 54, 1190-1193.

— (1970) Nickelian mackinawite from Vlakfontein, Transvaal - A reply. American Mineralogist, 55, 1807-1808.

Ward, C.J. (1970) The structure and properties of some iron sulphides. Reviews of Pure Applied Chemistry, 20, 175-206.

Watson, J.H.P., Ellwood, D.C., Deng, Q., Mikhalovsky, S., Hayter, C.E., and Evans, J. (1995) Heavy metal adsorption on bacterially produced FeS. Minerals Engineering, 8, 1097-1108.

Williams, A.J., McQueen, T.M., Ksenofontov, V., Felser, C., and Cava, R.J. (2009) The metal-insulator transition in $Fe_{1.01-x}Cu_xSe$. Journal of Physics-Condensed Matter, 21, 305701.

Wolthers, M., Van der Gaast, S.J., and Rickard, D. (2003) The structure of disordered mackinawite. American Mineralogist, 88, 2007-2015.

Zôka, H., Taylor, L.A., and Takeno, S. (1972) Compositional variations in natural mackinawite and the results of heating experiments. Journal of Science Hiroshima University, Series C, 7, 37-53.

Zajdel, P., Zubko, M., Kusz, J., and Green, M.A. (2010) Single crystal growth and structural properties of iron telluride doped with nickel. Crystal Research and Technology, 45, 1316-1320.

Zavašnik, J., Stanković, N., Arshad, S., and Rečnik, A. (2014) Sonochemical synthesis of mackinawite and the role of Cu addition on phase transformations in the Fe–S system. Journal of Nanoparticle Research, 16, 2223.

FIGURE CAPTIONS

Figure 1. Sites of incorporated transition metals in mackinawite (FeS). Sub – Fe substitution site; I-td – tetrahedral interstitial site between FeS sheets; I-sp site – square- pyramidal interstitial site.

Figure 2. Total energy vs *c* parameter of (a) FeS and (b) FeSe calculated using conventional DFT or DFT–D. Dotted lines represent experimental values of the *c* parameter.

Figure 3. Lattice parameters of $FeSe_{1-x}S_x$ vs S fraction (*x*). Dashed curves show the trends of calculated data using DFT–D. Experimental data (EXP) are from Mizuguchi et al. (2009).

Figure 4. Lattice parameters of (a) $Fe_{1-x}Co_xSe$, (b) $Fe_{1-x}Ni_xSe$, and (c) $Fe_{1-x}Cu_xSe$ vs. metal mole fraction (*x*). Dashed curves show the trends of calculated data using DFT–D. Experimental data (EXP) are from Thomas et al. (2009) in (a), Mizuguchi et al. (2009) in (b), and Willams et al. (2009) in (c).

Figure 5. DFT–D calculated (a) volume, (b) *a* (= *b*) axis parameter and (c) *c* axis parameter of $Fe_{1-x}Me_xS$ (Me = Co, Ni, or Cu) vs. metal mole fraction (*x*). Dashed curves show the trends of calculated data.

Figure 6. DFT–D calculated structures of $FeMe_xS$ (Me = Co, Ni, Cu) vs metal mole fraction (*x*) when Me occupies (a) the I-td (tetrahedral interstitial) site and (b) the I-sp (square-pyramid interstitial) site. Dashed curves show the trends of calculated data.

Figure 7. Formation energy (ΔE^f) of $Fe_{1-x}Me_xS$ (Sub, solid line) and $FeMe_xS$ (I-td, dashed line) vs chemical potential of sulfur ($\Delta\mu_S$) at 300 K (blue), 600 K (green), and 900 K (pink). Me = Co, Ni, or Cu; x = 0.125 or 0.25. $\Delta\mu_S = \mu_S - \mu_S^0$, where μ_S^0 is the chemical potential of S in the orthorhombic solid state. The ratio $p(H_2S)/p(H_2)$ corresponding to $\Delta\mu_S$ is shown in (c).

575 Table 1. Results of DFT–D geometry optimization of the structures of FeS and FeSe

	FeS			FeSe		
	NM	AFM	EXP[a]	NM	AFM	EXP[b]
$a=b$ (Å)	3.618	3.691	3.674	3.687	3.783	3.773
c (Å)	4.911	4.973	5.033	5.360	5.504	5.526
Fe–S (or Fe–Se) (Å)	2.185	2.242	2.256	2.319	2.399	2.395
Z_S (or Z_{Se}) (Å)	0.250	0.256	0.260	0.262	0.268	0.267
m_{Fe} (μ_B)	0	2.3	~1.0[c]	0	2.7	
E (meV/f.u.)	0	–82		0	–39	

576

577 *Notes*: NM and AFM represent respectively a non-magnetic state and an antiferromagnetic
578 ordering among Fe moments. EXP is an experimental value. Z_S (or Z_{Se}) is the fractional z-
579 coordinate of S (or Se). m_{Fe} is the magnetic moment size of Fe. E is the total energy relative
580 to that of NM FeS or FeSe per formula unit (f.u.).

581 [a] Lennie et al. (1995).
582 [b] McQueen et al. (2009).
583 [c] Kwon et al. (2011).

584

585

586

587

588 Table 2. Results of DFT–D geometry optimization of the structure of $FeNi_{0.125}Te$

	DFT–D		
	I-td	I-sp	EXP[a]
a (Å)	3.862	3.892	3.820
c (Å)	6.304	6.219	6.233
Z_{Te}	0.274	0.280	0.281
Z_{Ni}	0.500	0.693	0.710
E(meV)	+186	0	

589
590 *Notes*: Experiment (EXP) shows that in $FeNi_{0.125}Te$, Ni is at the I-sp (square-pyramid
591 interstitial) site instead of the I-td (tetrahedral interstitial) site. Z_{Te} and Z_{Ni} are the fractional z-
592 coordinates of Te and Ni, respectively. *E* is the total energy relative to that of I-sp.
593
594 [a]$FeNi_{0.1}Te$ (Zajdel et al., 2010).
595

596 Figure 1. Sites of incorporated transition metals in mackinawite (FeS). Sub – Fe substitution
597 site; I-td – tetrahedral interstitial site between FeS sheets; I-sp site – square-pyramidal
598 interstitial site.

599

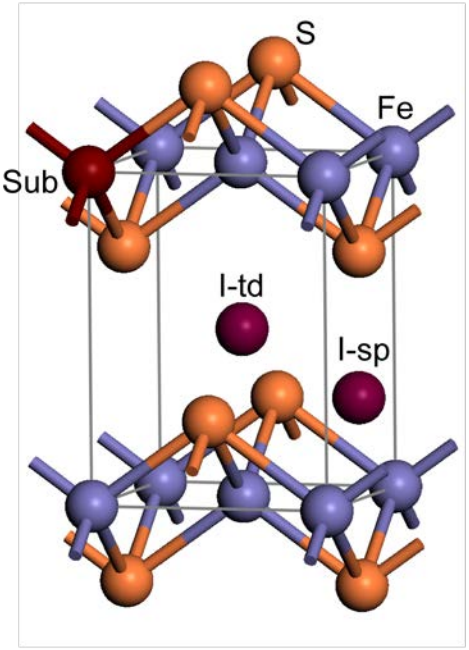

600
601
602

Figure 2. Total energy vs *c* parameter of (a) FeS and (b) FeSe calculated using conventional DFT or DFT–D. Dotted lines represent experimental values of the *c* parameter.

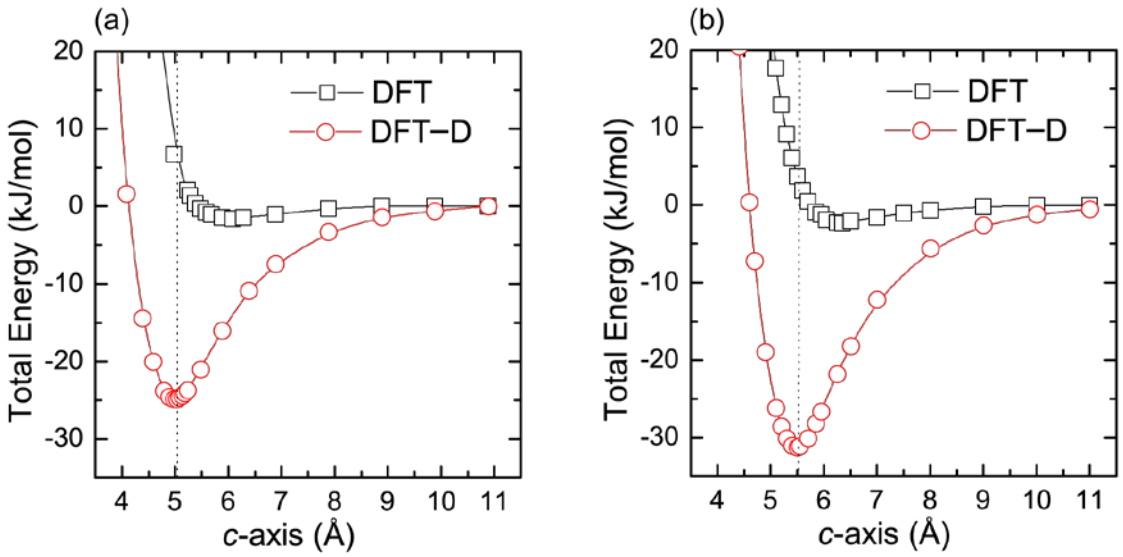

Figure 3. Lattice parameters of $FeSe_{1-x}S_x$ vs S fraction (x). Dashed curves show the trends of calculated data using DFT–D. Experimental data (EXP) are from Mizuguchi et al. (2009).

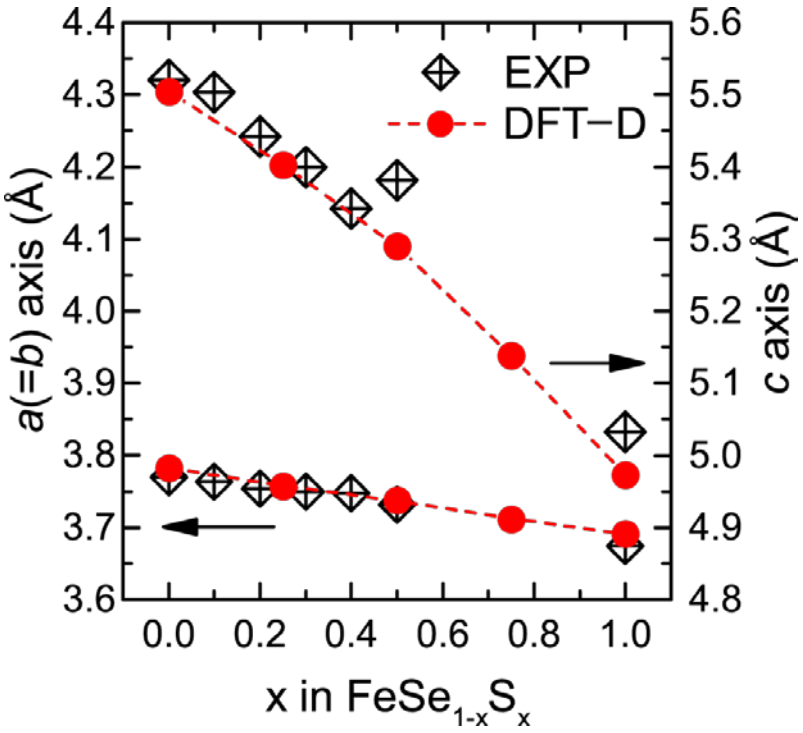

623 Figure 4. Lattice parameters of (a) $Fe_{1-x}Co_xSe$, (b) $Fe_{1-x}Ni_xSe$, and (c) $Fe_{1-x}Cu_xSe$ vs. metal
624 mole fraction (x). Dashed curves show the trends of calculated data using DFT–D.
625 Experimental data (EXP) are from Thomas et al. (2009) in (a), Mizuguchi et al. (2009) in (b),
626 and Willams et al. (2009) in (c).

627

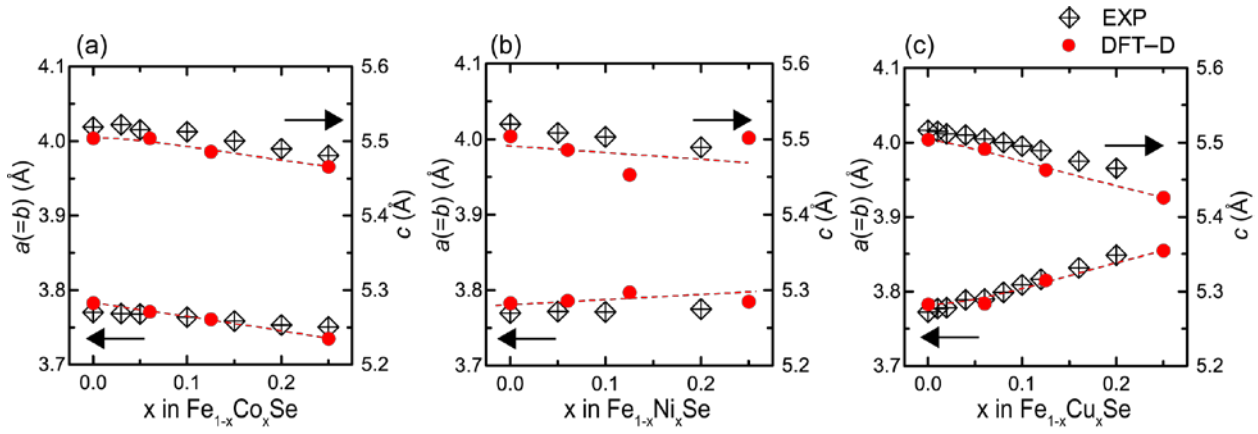

628

629

Figure 5. DFT–D calculated (a) volume, (b) *a* (= *b*) axis parameter and (c) *c* axis parameter of $Fe_{1-x}Me_xS$ (Me = Co, Ni, or Cu) vs. metal mole fraction (*x*). Dashed curves show the trends of calculated data.

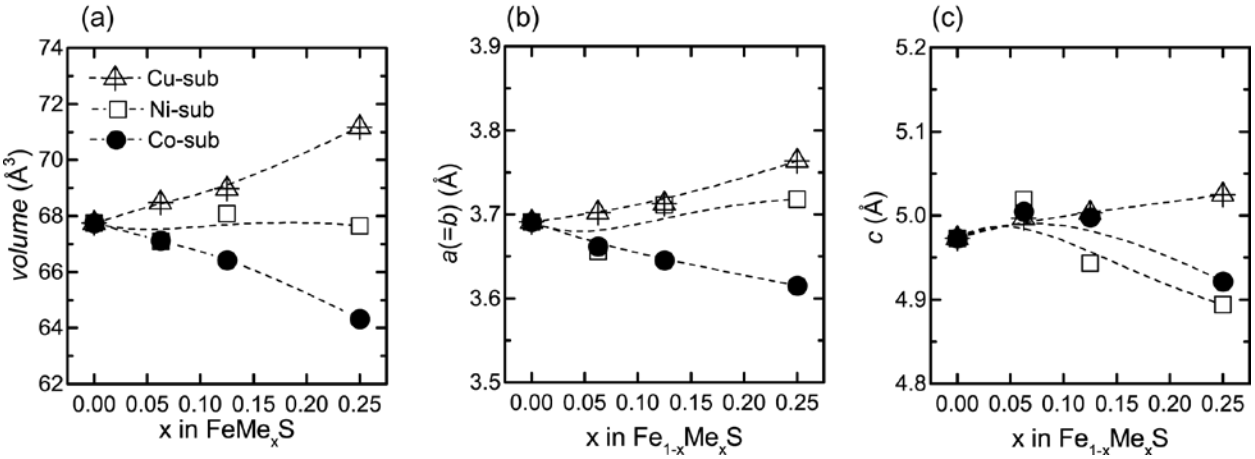

Figure 6. DFT–D calculated structures of $FeMe_xS$ (Me = Co, Ni, Cu) vs metal mole fraction (x) when Me occupies (a) the I-td (tetrahedral interstitial) site and (b) the I-sp (square-pyramid interstitial) site. Dashed curves show the trends of calculated data.

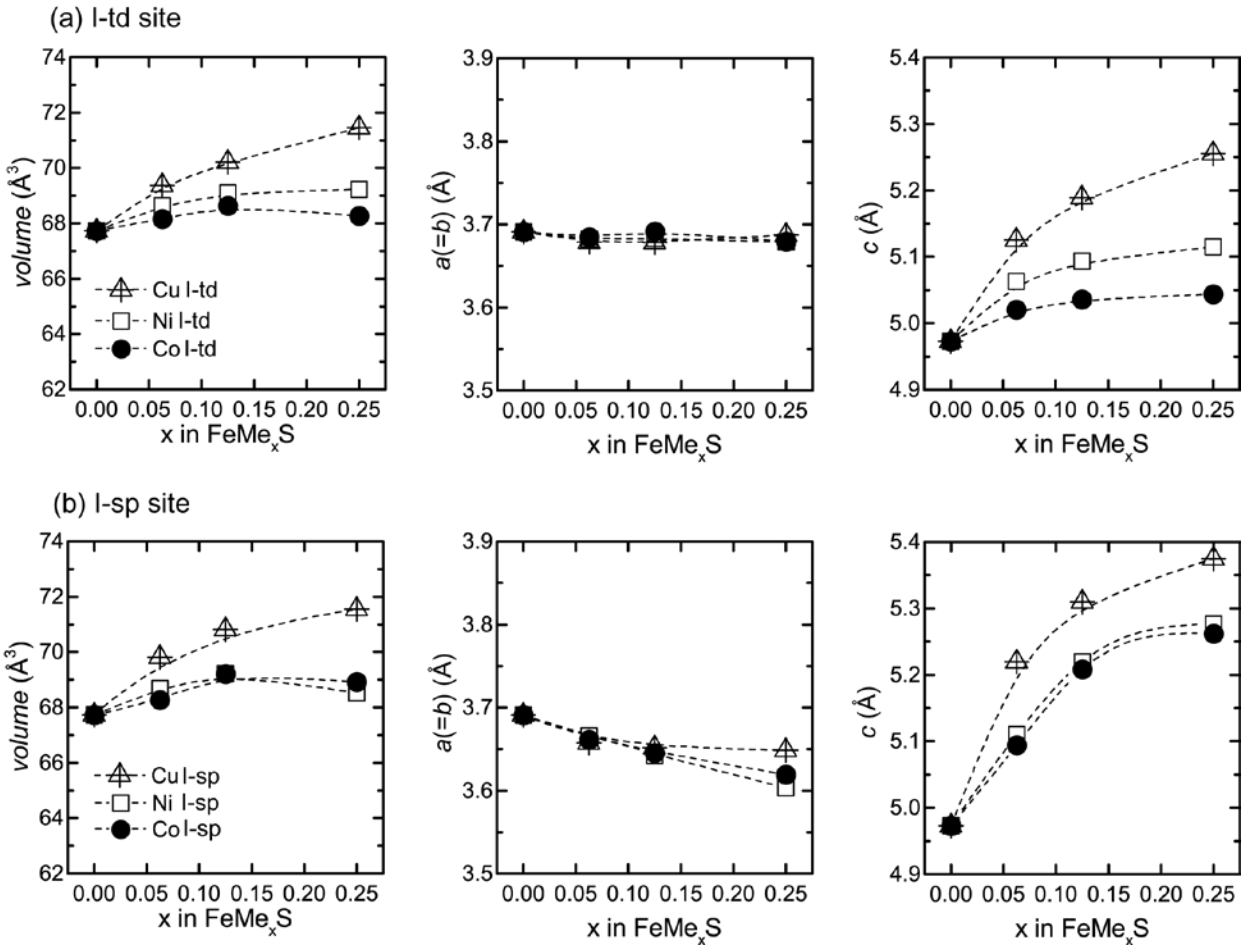

Figure 7. Formation energy (ΔE^f) of $Fe_{1-x}Me_xS$ (Sub, solid line) and $FeMe_xS$ (I-td, dashed line) vs chemical potential of sulfur ($\Delta\mu_S$) at 300 K (blue), 600 K (green), and 900 K (pink). Me = Co, Ni, or Cu; x = 0.125 or 0.25. $\Delta\mu_S = \mu_S - \mu_S^0$, where μ_S^0 is the chemical potential of S in the solid orthorhombic state. The ratio $p(H_2S)/p(H_2)$ corresponding to $\Delta\mu_S$ is shown in (c).